

# Hierarchical Time-Series Assessment and Control for Transient Stability Enhancement in Islanded Microgrids

Yang Shen<sup>ID</sup>, *Graduate Student Member, IEEE*, Yelun Peng<sup>ID</sup>, *Member, IEEE*, Zhikang Shuai<sup>ID</sup>, *Senior Member, IEEE*, Quan Zhou<sup>ID</sup>, *Senior Member, IEEE*, Lipeng Zhu<sup>ID</sup>, *Member, IEEE*, Z. John Shen<sup>ID</sup>, *Fellow, IEEE*, and Mohammad Shahidehpour<sup>ID</sup>, *Life Fellow, IEEE*

**Abstract**—The grid-forming converters would integrate battery energy storage systems (BESSs) in islanded microgrids for smoothing out the uncertain fluctuations of renewable energy resources. However, grid-forming converters would pose transient instability risks under large disturbances, which could require fast and accurate stability assessment methods in such challenging and uncertain cases. In this work, a hierarchical time-series assessment and control (HTSAC) framework is proposed for assessing the transient stability of grid-forming converters in islanded microgrids. The proposed HTSAC framework offers a gated recurrent unit (GRU) neural network alternative for an intuitive and accurate trajectory prediction in early post-fault stages. Subsequently, an emergency ride-through control (ERC) strategy is proposed which leverages the proposed neural network approach for enhancing the prediction results in real-time assessments of microgrid transient stability. The initial input horizon of GRU is optimized to avoid intense trial-and-error design burdens incurred in conventional data-driven assessment methods. Simulation and experimental results are presented to validate the effectiveness of the proposed HTSAC on an islanded microgrid in south China. The results also point out that the GRU of the prediction layer with a quantile loss function would ensure a timely ERC in the proposed HTSAC approach to renewable energy-based converter operations.

**Index Terms**—Islanded microgrids, grid-forming converters, gated recurrent unit neural network, renewable energy integration, transient stability assessment, emergency control.

Manuscript received 31 May 2022; revised 2 November 2022 and 15 December 2022; accepted 10 January 2023. Date of publication 18 January 2023; date of current version 23 August 2023. This work was supported in part by the National Natural Science Foundation of China under Grant 52125705 and Grant G2022160028L, and in part by the Key-Area Research and Development Program of Hunan Province, China, under Grant 2021SK2051. Paper no. TSG-00776-2022. (Corresponding authors: Yelun Peng; Mohammad Shahidehpour.)

Yang Shen, Yelun Peng, Zhikang Shuai, Quan Zhou, and Lipeng Zhu are with the College of Electrical and Information Engineering, Hunan University, Changsha 410082, China (e-mail: shenyang96@hnu.edu.cn; pengyelun@163.com; szk@hnu.edu.cn; zquan@hnu.edu.cn; zhulpwhu@126.com).

Z. John Shen is with the School of Mechatronic Systems Engineering, Simon Fraser University, Surrey, BC V3T 0A3, Canada (e-mail: johnshen@ieee.org).

Mohammad Shahidehpour is with the Electrical and Computer Engineering Department, Illinois Institute of Technology, Chicago, IL 60616 USA (e-mail: ms@iit.edu).

Color versions of one or more figures in this article are available at <https://doi.org/10.1109/TSG.2023.3237965>.

Digital Object Identifier 10.1109/TSG.2023.3237965

## NOMENCLATURE

### Abbreviations

BESS	Battery storage energy system
CNN	Convolutional neural network
ERC	Emergency ride-through control
GFC	Grid-forming converters
GRU	Gated recurrent unit
HTSAC	Hierarchical time-series assessment and control
LSTM	Long-short term memory
MAE	Mean absolute error
MLP	Multilayer perception neural network
$R^2$	R-squared
TSA	Transient stability assessment

### Symbols

$b$	Bias matrices
$C_f$	Capacitor of filter
$D_p$	Droop coefficient for active power loop
$D_q$	Droop coefficient for reactive power loop
$E$	Voltage amplitude
$h_t$	Hidden gate state of GRU
$J$	Virtual inertia
$L_f$	Converter filter inductance
$P_0$	Active power reference
$P_{em}$	Active output power
$r_t$	Reset gate state of GRU
$T_{IH}$	Calculated input time horizon
$T_s$	Sample interval of virtual power angle
$W$	Weight matrices of GRU
$x_t$	Input state of GRU
$z_t$	Update gate state of GRU
$\gamma$	Quantile ratio of loss function
$\delta$	Virtual power angle
$\varepsilon_i$	Adjustment ratio of ERC
$\omega$	Angular speed.

## I. INTRODUCTION

POWER electronic converters play vital roles in integrating renewable energy resources, such as photovoltaic and wind power, into islanded microgrids [1], [2]. The grid-forming converters with virtual inertia are proposed [3], [4]

as the battery energy storage system (BESS) interface to regulate system frequency while flattening the fluctuation caused by uncertain renewable energy resources [5]. However, large disturbances like three-phase ground faults and line outages could cause grid-forming converters to lose synchronism with the network. Moreover, transient instability could occur much faster in islanded microgrids as compared with those connected to distribution networks [6], [7]. Therefore, transient stability assessment (TSA) of grid-forming converters is critically important for islanded microgrids, which can ensure an accurate evaluation and timely emergency ride-through control (ERC) for maintaining the converter stability after large disturbances.

Conventionally, TSA is carried out via time-domain simulations and Lyapunov energy function evaluations, which could be impractical for islanded microgrids. Time-domain simulations are the most widely used TSA method for its accuracy, which suffers from heavy computational requirements in online applications, though there are some efforts to reduce the TSA model complexity [8] and optimize the algorithm [9] for real-time applications. The Lyapunov energy function-driven TSA is based on the priori knowledge of transient mechanism whose calculation speed is fast enough to support online applications. However, the Lyapunov function lacks a concise TSA approach, which could limit its application to converter-based systems [10], [11]. A neural Lyapunov approach with a risk-minimize loss function is proposed in [12] to mitigate this gap, which combines the data-driven method with the transient stability mechanism to reduce its conservatism in TSA applications. But most Lyapunov function evaluations could rely on tools such as linear matrix inequalities [13], which are inapplicable when considering converter overcurrent limitations because the saturated limiter would induce a continuous non-differentiable operating point.

The key TSA properties are acquiring the system stability accurately and expeditiously. In this view, machine learning technologies provide opportunities for intelligent TSA from a data-driven perspective. A full-connected neural network TSA is established to assess the system stability after fault [14]. Excellent online TSA applications have been reported recently, including decision trees [15], support vector machines [16], and extreme learning machines [17]. However, most of these machine learning-driven TSA methods only estimate stability criteria rather than providing quantitative assessments of such outcomes. Additionally, their performances rely on manual feature selections, which make it even more difficult in islanded microgrid applications considering the complexity of massively populated converters.

End-to-end neural networks present their superiority in fitting complex nonlinear functions in which the impact of feature selection in dynamic performances would be reduced. There are two mainstream classes of neural networks which are considered as core TSA algorithms. One is the convolutional neural network (CNN) [18] and its improved variants [19]. The system is modeled as a two-dimensional map, with the input data horizon and kernel size determined by trial and error. The other is the recurrent neural network (RNN), with two popular core algorithms, which include

long short-term memory (LSTM) and gated recurrent unit (GRU). In [20], [21], the LSTM neural network is utilized to assess the dynamic stability accurately. Similar to the CNN-based TSA methods, critical hyperparameters of LSTM-based TSA methods, like input data horizon, are achieved using time-consuming parameter tuning procedures or individual experiences [22]. Considering the proliferation of power converters in islanded microgrids, the assessment performance cannot be guaranteed and hardly transferred to other scenarios.

However, the solution gaps still exist in the majority of TSA methods: TSA and ERC are considered separately rather than in a closed-loop framework. This issue could endanger the stable operations of islanded microgrids because their transient process is much faster than that in bulk power systems. The widely-used emergency control is a predefined control set in which online situations are rarely considered. Only a few works take a joint perspective to leverage assessment results for guiding and quantizing the emergency control strategies such that the stability of islanded microgrids is enhanced adaptively. For example, emergency control actions are taken according to different unstable mode outputs by the CNN-based TSA method [23], but the control strategies are still predefined. Similar work is reported in [24], [25]. Control strategies are proposed in [26] by assuming that the stability is known. Reference [27] presents an idea that is similar to this work, but there are two main gaps: first, detailed load-shedding strategies are not based on assessment results, and second, the control action is based on the current state. These postulates are assumed practical in bulk power systems but face serious risks in islanded microgrids considering their faster rates of losing synchronism.

The existing research gaps are summarized as follows: conventional TSA can only identify whether or the system is stable, which is not enough to characterize islanded microgrids with strong nonlinearity; data-driven TSA can fit complex dynamic behaviors but requires time-consuming trial-and-error steps to optimize parameters; most importantly, TSA and ERC are considered separately, making it difficult to adaptively stabilize microgrids in a very short time. The comparisons among the stated literature studies are summarized in Table I.

To fill these research gaps, TSA and online ERC strategy are considered jointly to form a comprehensive framework in this paper. A gated recurrent unit (GRU) neural network-based TSA layer and ERC layer are included to establish the hierarchical time-series assessment and control (HTSAC) framework. The framework requires only one input feature to assess the transient stability of converters rapidly and accurately, followed by an effective online adaptive ERC based on the assessment results. The contributions of this work are outlined as follows:

- (1) An HTSAC framework is proposed to predict the high-precision trajectory of virtual power angle using temporal data which derive the ERC strategy adaptively. Different from most existing methods that only determine microgrid stability qualitatively, the proposed continuous trajectory prediction by the TSA layer can intuitively guide the subsequent emergency control quantitatively.

TABLE I  
COMPARISON OF EXISTING PAPERS REVIEWED IN THIS WORK

Reference	Features					
	Feature set selection sensitive	Time-series data processing	Optimal parameter design	Quantitative assessment result	Corresponding emergency control	Adaptability in islanded microgrids
T. Huang & et al. [12]	✗	✗	✓	✗	✗	✗
D. Sobajic & et al. [14]	✓	✗	✗	✓	✗	✓
T. Guo & et al. [15]	✓	✗	✗	✗	✗	✗
W. Hu & et al. [16]	✓	✗	✗	✗	✗	✗
Q. Li & et al. [17]	✓	✗	✗	✗	✗	✓
A. Gupta & et al. [18]	✗	✓	✗	✗	✗	✓
X. Li & et al. [19]	✗	✓	✗	✗	✗	✓
B. Li & et al. [20]	✗	✓	✗	✗	✗	✓
J. Yu & et al. [21]	✗	✓	✓	✗	✗	✓
J. Gonzalez & et al. [22]	✗	✓	✗	✗	✗	✓
Z. Shi & et. al. [23]	✗	✓	✗	✗	✗	✓
J. Pinzón & et al. [24]	✗	✓	✗	✗	✗	✗
A. Singh & et al. [25]	✗	✓	✗	✗	✗	✗
S. Siddiqui & et al. [26]	✗	✗	✗	✗	✗	✗
Q. Wang & et al. [27]	✗	✓	✗	✓	✓	✗
<b>This work</b>	✗	✓	✓	✓	✓	✓

- (2) The time scale of the converter's power control loop is calculated to optimize the input horizon length of the TSA layer, which eliminates the time-consuming tuning procedure and enhances the portability. The proposed HTSAC framework ensures the accurate prediction of transient stability while the conservation of the prediction is minimized by the quantile loss function.
- (3) A real-time adaptive ERC strategy is proposed by leveraging the predicted trajectory. Aiming at enhancing the transient stability of grid-forming converters, the active power control loop of the converter is adjusted according to the predicted results to increase the deceleration area of grid-forming converters and thus provide a comprehensive transient stability enhancement solution.

The remainder of this paper is organized as follows. In Section II, the grid-forming converter control strategy and the GRU algorithm are briefly reviewed. In Section III, the proposed HTSAC framework is established and optimized from the perspective of the physical properties of transient stability issues. Subsequently, the adaptive ERC strategy is proposed utilizing the prediction result. Experiments and comparative tests are presented in Section IV on an islanded microgrid in south China and a 38-bus microgrid. Section V concludes the whole work.

## II. PRELIMINARIES

The lack of converter inertia and quick response characteristics could lead to fault propagation, which demands an extremely high speed HTSAC framework for converters in microgrids with high-penetration renewable energy. Preliminaries required to establish the proposed HTSAC framework will be introduced in this section.

### A. Converter Control Scheme

BESS is often integrated into islanded microgrids to offer virtual inertia and damping through grid-forming converters. The control scheme of the grid-forming converters with over-current limitation methods is illustrated in Fig. 1. The power

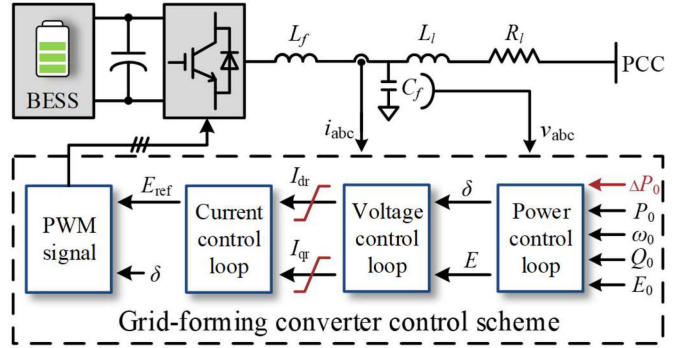


Fig. 1. Topology and control scheme of the grid-forming converter integrating the BESS into the microgrid.

control loop of grid-forming converters discussed in this paper will provide virtual inertia [10]. We assume the current limitation is not saturated during a fault such that the grid-forming converters can support the islanded microgrid. If define the virtual power angle  $\delta$  as the angle between local and system coordinates, then

$$\frac{d\delta}{dt} = \omega - \omega_0 \quad (1)$$

$$J \frac{d^2\delta}{dt^2} = P_0 - P_{em} - D_p(\omega - \omega_0) \quad (2)$$

where  $\omega$  is the angular speed of the converter, and  $\omega_0$  is the rated angular speed of microgrid.  $D_p$  is the active damping coefficient,  $P_0$  is the active power reference, and  $P_{em}$  is the active output power. The first-swing stability is used for simplicity to analyze the transient stability issue. With the existence of the current limitation, the mathematical model of HTSAC is nonlinear and upper or lower bounds of current limiters form singular points of the model. The linear matrix inequalities method is one of the most promising methods to construct the above-mentioned energy function, though it cannot handle models with a singular point, as manifested by its name. Moreover, voltage changes during a fault could also influence the unstable equilibrium point. Though the influence

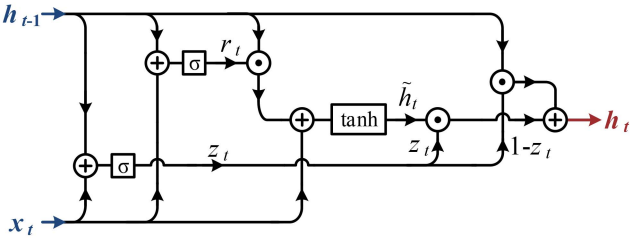


Fig. 2. Structure of a GRU neural network cell at the  $t$  step where the circle with a dot means Hadamard product and the circle with a cross means concatenate.

on the unstable equilibrium point is limited, voltage dynamics are ignored here because the transient stability refers to large disturbances. Hence, virtual power angles are selected as a more effective input when compared to voltage because voltage dynamics are implied in the changes of virtual power angle. Accordingly, the GRU neural network is leveraged to possess the temporal virtual power angle data and assess the nonlinear dynamic behavior of virtual power angles in this work.

### B. GRU Neural Network Algorithm

GRU neural network is one of the outstanding representatives of recurrent neural networks. As a derivative of recurrent neural network [28], GRU fits high-dimensional nonlinear functions well, with a faster training convergence capability. The structure of GRU is depicted in Fig. 2, which consists of three parts (i.e., gates) [29]. The update gate which is denoted as “ $z_t$ ” is the controller at the  $t$  step that determines the amount of retained information from the last step hidden state  $h_{t-1}$  to current step  $h_t$ , as described in (3). The reset gate which is denoted as “ $r_t$ ” is relatively complex. The  $r_t$  value is determined by the input  $x_t$  and the last step hidden state  $h_{t-1}$ . Subsequently, the candidate hidden state of the current step is calculated with  $r_t$ ,  $h_{t-1}$ , and  $x_t$ . The candidate hidden state is the intermediate GRU step, which is stated as

$$z_t = \sigma(W_z \cdot [h_{t-1}, x_t] + b_z) \quad (3)$$

$$r_t = \sigma(W_r \cdot [h_{t-1}, x_t] + b_r) \quad (4)$$

$$\tilde{h}_t = \tanh(W_h \cdot [r_t \cdot h_{t-1}, x_t] + b_h) \quad (5)$$

The hidden state  $h_t$  is calculated in every step

$$h_t = (1 - z_t) \cdot h_{t-1} + z_t \cdot \tilde{h}_t \quad (6)$$

It should be noted that  $\sigma$  and  $\tanh$  refer to sigmoid function and hyperbolic tangent function, respectively.  $W$  stands for weight matrices and  $b$  for bias matrices. Training and calculating GRU are the state updating processes.

Different from the cell state that is used in the long-short term memory neural network, GRU carries information through a hidden state which is used as the output of GRU at the last step. By unfolding the GRU cell along the temporal dimension, neural network constitutes a chain-like structure that enables the outstanding performance of nonlinear function fitting process by passing the information along the chain.

### III. PROPOSED HTSAC FRAMEWORK

The proposed HTSAC framework consists of two layers: a high-precision virtual power angle trajectory prediction layer based on the GRU neural network and an adaptive ERC layer based on the transient stability mechanism. The adaptive ERC strategy leverages the prediction result of the GRU neural network. This section describes the establishment and the optimization of the HTSAC framework.

#### A. Implementation of the HTSAC framework

The details of the proposed HTSAC framework are shown in Fig. 3. First, only the virtual power angle of each grid-forming converter is collected periodically. The interval of data collection is equal to the input horizon length of the prediction layer, which will be discussed and optimized offline in Section III-B. For online applications, the virtual power angle data at every interval are pre-processed and sent into the high-precision trajectory prediction layer based on GRU neural network. The prediction layer is operated online and recurrently assessed if the grid-forming converter is stable in the next time horizon. Once the grid-forming converter is predicted to be unstable, the HTSAC framework transmits the predicted trajectory into the ERC layer. The ERC layer calculates adaptive ride-through control action to enhance the grid-forming converter stability.

Virtual power angle data are normalized first to eliminate the effect of abnormal data and maintain the performance of the HTSAC framework in various scenarios. Also, appropriate evaluation can reflect the performance of the HTSAC framework effectively. The data pre-processing method and the evaluation metrics mentioned above are presented as follows.

The input data are normalized at first with the min-max normalization method, which are stated as:

$$x'_i = \frac{x_i - x_{\min}}{x_{\max} - x_{\min}} \quad (7)$$

where  $x_i$  is the element in the input data  $x_t$ .

The mean absolute error and the R-squared are chosen to estimate the prediction layer performance. For the sake of brevity, the mean absolute error (denoted as  $MAE$ ) and the R-squared (denoted as  $R^2$ ) are listed as (8) and (9), respectively.  $MAE$  will evaluate the accuracy of trained GRU, where the smaller  $MAE$  represents a closer predicted value to the real value.  $R^2$  reflects the goodness of model fit, where, from a statistical point of view,  $R^2$  would be closer to 1 for a better-fitted regression equation.

$$MAE = \frac{1}{n} \sum_{i=1}^n |y_i - \tilde{y}_i| \quad (8)$$

$$R^2 = 1 - \frac{\sum_{i=1}^n (y_i - \tilde{y}_i)^2}{\sum_{i=1}^n (\bar{y}_i - \tilde{y}_i)^2} \quad (9)$$

#### B. Input Horizon Optimization

The optimization of the input horizon can be seen as a trade-off between the precision and the execution time of the GRU-based prediction. On the one hand, the longer the input horizon is, the more information will be passed into the neural network.

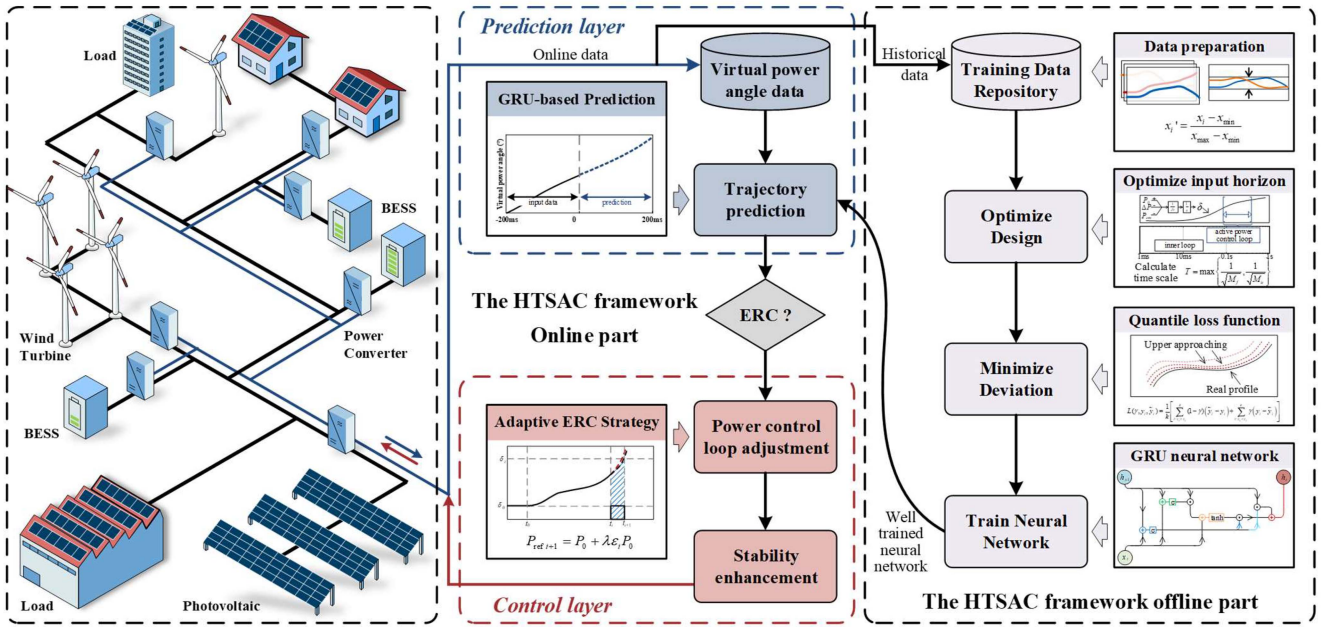


Fig. 3. Structure of the proposed HTSAC framework.

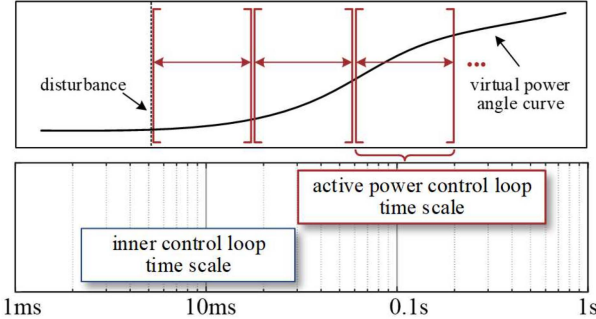


Fig. 4. Illustration of the active power control loop time scale and its figurative expression on the virtual power angle curve.

On the other hand, the redundant information requires high-performance hardware which results in a slower calculation speed.

The well-designed input horizon of the GRU neural network is the premise of fast and accurate trajectory prediction. However, few literature studies have discussed this subject in which the input horizon is often determined simply by experience [18], [20] or by the grid-search method [22]. This time-consuming and low-efficient design will be cumbersome when transferring the trained HTSAC framework to a grid-forming converter with new control parameters.

Since the transient behavior of virtual power angle is mainly concerned with the power control loop, the input horizon design can be tailored quantitatively within the active power control loop time scale. Accordingly, a quantitative method that differs from the commonly-used grid-search method is applied, as illustrated in Fig. 4. By calculating the time scale, the input horizon is spared from the time-consuming trial-and-error method as validated by the experiment result presented in Section IV.

This section focuses on optimizing the input horizon, which is calculated as follows. Define a second-order differential equation as [30]:

$$\ddot{x} = f(x(t), \dot{x}(t), w, u) \quad (10)$$

where  $w$  is the disturbance and  $u$  is the input. Assume the bounded changes of  $x$ , the derivative of  $x$ , and the disturbance obey the following:

$$|x| < v_1, |\dot{x}| < v_2, |w| < v_w, |u| < \zeta \quad (11)$$

where  $v_1, v_2, v_w$  are ranges of variables, and  $\zeta$  is the range of input variable. In this work, active power can be seen as input variable, which is inherently a bounded variable that is constrained by output current limitation. Then the time scale  $T_{IH}$  is calculated as follows.

$$\begin{cases} M_1 = \max|f(x, \dot{x}, w, u)|, u = 0 \\ M_2 = \max|f(x, \dot{x}, w, u) - f(x, \dot{x}, w, 0)|, u \neq 0 \cup |u| < \zeta \end{cases} \quad (12)$$

$$T_{IH} = \max\left\{\frac{1}{\sqrt{M_1}}, \frac{1}{\sqrt{M_2}}\right\} \quad (13)$$

The detailed sampled values of a grid-forming converter are listed in Table II. Reorganize the power control loop as:

$$\ddot{\delta} = -\frac{1}{J}\left(\frac{k_p}{\omega_0} + D_p\right)\dot{\delta} + \frac{1}{J}\left(\frac{P_0}{\omega_0} + k_p + D_p\omega_0\right) - \frac{1}{J\omega_0}P \quad (14)$$

For a grid-forming converter, it is required to continuously provide active power output to support the system during fault, which means the input variable  $u \neq 0$ . The time scale  $T_{IH}$  is calculated as:

$$T_{IH} = \frac{1}{\sqrt{M_2}} = \left| -\frac{1}{J}\left(\frac{k_p}{\omega_0} + D_p\right)\dot{\delta} + \frac{1}{J}\left(\frac{P_0}{\omega_0} + k_p + D_p\omega_0\right) \right| \quad (15)$$

TABLE II  
DETAILED PARAMETERS OF A GRID-FORMING CONVERTER

Key Parameters	Values
Reference angular speed ( $\omega_0/\omega_g$ )	314.159 rad/s
Reference voltage magnitude ( $E^*$ )	311 V
Rated active power ( $P^*$ )	20 kW
Rated reactive power ( $Q^*$ )	5 kVar
Inertia value ( $J$ )	5
$P-f$ droop coefficient ( $D_p$ )	8
$Q-V$ droop coefficient ( $D_q$ )	166
Inductance of filter ( $L_f$ )	0.1 p.u.
Capacitor of filter ( $C_f$ )	0.1 p.u.
Speed governor coefficient ( $k_p$ )	12

$$\begin{aligned} & -\frac{1}{J\omega_0} - f(x, \dot{x}, w, 0) \Big| \\ &= \left( \max \left| -\frac{1}{J\omega_0} P \right| \right)^{-\frac{1}{2}} \end{aligned} \quad (15)$$

Set  $\zeta = 2P_0$ , the time scale of active power control loop is equal to 0.202s according to (14)-(15).

### C. Loss Function Design

In this part, the loss function selection for training the prediction layer and the present convergence validation of the quantile loss function are discussed.

The loss function is utilized to measure the deviation between the prediction and the actual profile during the training and enhance the accuracy of the neural network. Since the prediction of the virtual power angle is essentially a regression issue, various functions like mean squared error loss, mean absolute error loss, etc. are considered candidates. Though these loss functions are widely used and proved effective, they only instruct neural network training without considering the converging direction. To deal with this shortcoming, the quantile loss function is utilized in this work as discussed next.

Denote the real profile as  $\mathbf{Y}$  and the prediction as  $\tilde{\mathbf{Y}}$ . Both  $\mathbf{Y}$  and  $\tilde{\mathbf{Y}}$  are vectors of length  $k$ , where  $k$  is the prediction horizon. Define the estimation error vector  $\Delta \mathbf{Y}$  as:

$$\Delta \mathbf{Y} = \mathbf{Y} - \tilde{\mathbf{Y}} = [\Delta y_1, \Delta y_2, \dots, \Delta y_k]^T \quad (16)$$

For those loss functions without considering convergence directions like mean squared error and mean absolute error, the deviations are

$$\Delta \mathbf{Y}_{MSE} = \frac{1}{k} \sum_{i=1}^k \Delta y_i^2 \quad (17)$$

$$\Delta \mathbf{Y}_{MAE} = \frac{1}{k} \sum_{i=1}^k |\Delta y_i| \quad (18)$$

Since the values are non-negative, the neural network is unable to judge whether its prediction has overvalued or underestimated the real profile during every training epoch. As long as the gap between the prediction and the real profile is the same, the deviation effect would be the same for the neural network, as illustrated in Fig. 5. This brings an uncontrollable risk, where the GRU neural network becomes a black box predictor of underestimating or overvaluing.

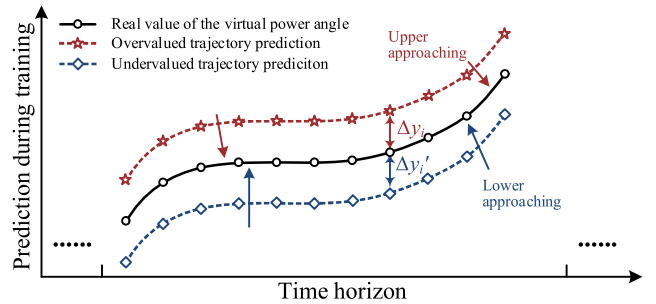


Fig. 5. Converging process when training GRU neural network under the guidance of quantile loss. By tuning the parameter  $\gamma$  of the quantile loss function, the prediction layer based on GRU neural network will approach from upper side of the real profile to ensure the transient stability of microgrids.

Consider an extreme case, where the neural network predicts a critical profile on the edge of losing stability. The GRU neural network trained with the mean squared error underestimates the real profile, which causes the miss-detection of the unstable grid-forming converter. The grid-forming converters are essential in microgrids in that they often provide voltage and frequency support for other converters. If the transient instability is not properly detected, it can cause the collapse in the microgrid network operation. Also, if the virtual power angle is overvalued, it might cause a false alarm for implementing the ERC strategy on stable converters. Comparing the two situations, we learn that the former case is much more serious.

In this work, the quantile loss function is leveraged to train the prediction layer so that it can converge from the upper side of the real profile with minimum deviation. The convergence speed of the quantile loss function is faster than that of the mean squared error function, which can shorten the training process of the neural network. The quantile loss function is constructed as

$$L(\gamma, y_i, \tilde{y}_i) = \frac{1}{k} \left[ \sum_{i: \tilde{y}_i \geq y_i}^k (1-\gamma)(\tilde{y}_i - y_i) + \sum_{i: \tilde{y}_i < y_i}^k \gamma(y_i - \tilde{y}_i) \right] \quad (19)$$

where  $\gamma$  stands for the quantile ratio which provides distinct overestimation and underestimation penalties such that the HTSAC preference is ensured. When  $\gamma > 0.5$ , the overestimation of the prediction value suffers fewer penalties during training, thus the GRU neural network prefers to converge from the upper side of the real profile, and vice versa.

Another issue that should be considered is the convergence of the loss function. Assume the training dataset is  $X$ . To achieve the least conservative HTSAC framework estimation, the training process is essentially equal to finding the most suitable GRU neuron weight matrix that would minimize [31],

$$\min_{\gamma} L(\gamma, y_i, \tilde{y}_i) \quad (20)$$

*Definition 1:* A function  $f: \mathbb{R}^n \rightarrow \mathbb{R}$  is *convex* if  $\text{dom } f$  is a convex set and if for all  $x, y \in \text{dom } f$ , and  $\mu$  with  $0 \leq \mu \leq 1$ , there is

$$f(\mu x + (1-\mu)y) \leq \mu f(x) + (1-\mu)f(y) \quad (21)$$

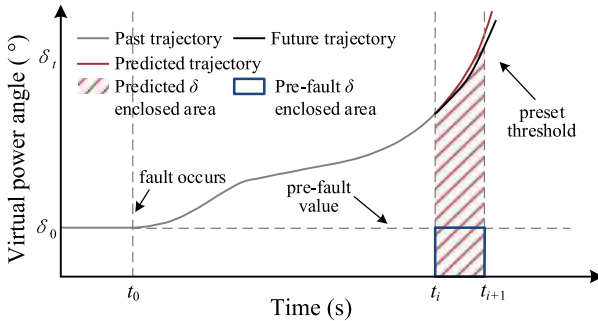


Fig. 6. Illustration of the proposed ERC strategy.

Correspondingly, the first-order condition of the definition is derived as

*Property 1:* Suppose the gradient of  $f$  exists for all  $x, y \in \text{dom } f$  (which is also convex), then function  $f$  is convex if and only if

$$f(y) \geq f(x) + \nabla f(x)^T (y - x) \quad (22)$$

Either  $\mathbf{Y}$  or  $\tilde{\mathbf{Y}}$  is a set of real numbers which is a convex subset of a real vector space. Consider the inequality below

$$L(\gamma, y_i, \tilde{y}_i)|_{\mathbf{Y}} \geq L(\gamma, y_i, \tilde{y}_i)|_{\tilde{\mathbf{Y}}} + \nabla L(\gamma, y_i, \tilde{y}_i)^T|_{\tilde{\mathbf{Y}}} \cdot \Delta \mathbf{Y} \quad (23)$$

For all  $\mathbf{Y}$  and  $\tilde{\mathbf{Y}}$ , (23) always holds which denotes that  $L$  is a convex function. A convex function can be optimized by leveraging the gradient descent algorithm. Though the existence of the activation function makes the optimization process non-convex, the HTSAC framework converges to local minima. But this problem can be mitigated by conducting multiple iterations of training or optimizing the choice of initial weights. Therefore, the conservation of the proposed HTSAC framework will be reduced according to the quantile loss.

#### D. Adaptive ERC Strategy

In this part, the adaptive ERC strategy utilizing the information predicted by the GRU neural network is presented. Increasing the deceleration area and decreasing the acceleration area of the grid-forming converter would be helpful for riding-through faults and enhancing its transient stability according to the transient stability mechanism.

Under normal operations, the control scheme is the same as that depicted in Fig. 1 and the detailed control parameters remain unchanged. When the fault occurs, the GRU-based prediction layer starts to cycle working when receiving the fault signal. Once the prediction shows that there is a possibility of exceeding the threshold, an additional item  $\Delta P_0$  is implemented in the power control loop. Thus, the adaptive ERC instructs the converter to decrease its reference active power  $P_{\text{ref}}$  in the next time interval, as shown in Fig. 6 and (24).

$$P_{\text{ref}i+1} = P_0 + \lambda \Delta P_0 = P_0 + \lambda \varepsilon_i P_0 \quad (24)$$

where  $\lambda = 1$  if and only if the fault occurs, otherwise  $\lambda = 0$ . Denote the sample interval of virtual power angle as  $T_s$ ,  $\varepsilon_i$  is

---

#### Algorithm 1 HTSAC Framework Algorithm

---

```

1: function Pred( $\delta(t)$ )
2:   if  $\delta(t) < \pi/2$ 
3:     ERCStart = 0;
4:   else if  $\delta(t)_{\text{max}} = \delta(t)_{\text{end}}$  do
5:     Pre-process the virtual power angle  $\delta(t)$  by (7)
6:     Calculate  $\delta_{\text{pred}}(t+1)$  by GRU( $\delta(t)$ ) via (3) —(6)
7:   end if
8:   if  $\delta_{\text{pred}}(t+1) > \pi/2$ 
9:     Update ERCStart: ERCStart  $\leftarrow 1$ 
10:    else Update ERCStart: ERCStart  $\leftarrow 0$ 
11:   end if
12: end if
13: return  $\delta_{\text{pred}}(t+1)$ , ERCStart
14: end function Pred
15: function ERC( $\delta_{\text{pred}}(t+1)$ , ERCStart)
16:   Set tripoff and fault signal with Tripoff = 0,  $\lambda = 1$ 
17:   if  $\delta_{\text{pred}}(t+1) > \pi$ 
18:     Update Tripoff signal with Tripoff  $\leftarrow 1$ 
19:     Break
20:   else if ERCStart
21:     Compute  $\varepsilon_i$  by (25) with  $\delta_{\text{pred}}(t+1)$ 
22:     Compute  $P_{\text{ref}i+1}$  with  $P_0 + \lambda \varepsilon_i P_0$  via (24)
23:   end if
24:   return Tripoff,  $P_{\text{ref}i+1}$ 
25: end function
```

---

the coefficient that is calculated as

$$\varepsilon_i = 1 - \frac{\int_{t_i}^{t_{i+1}} \delta_0 dt}{\int_{t_i}^{t_{i+1}} \delta_p dt} = 1 - \frac{\delta_0(t_{i+1} - t_i)}{\sum_{j=1}^{\tau} (\delta_p^j \cdot T_s)} \quad (25)$$

where  $t_i$  is the end time of the  $i$  th time window which is also the start of the  $i+1$  th in the future,  $\tau = T / T_s$ .  $\varepsilon_i$  can be recognized as the ratio of the area enclosed by the virtual power angle  $\delta_0$  when the pre-fault operation is divided by the predicted curve enclosed area. It reflects the danger level of the microgrid to some extent in the next time window. Algorithm 1 demonstrates how the adaptive ERC utilizes trajectory information predicted by the GRU neural network.

#### IV. CASE STUDIES

The flowchart of the proposed HTSAC framework is illustrated in Fig. 7. A real islanded microgrid of south China and a 38-bus microgrid [32] are leveraged as the test system, as illustrated in Figs. 8 and 9, respectively, to fully verify the performance of the proposed framework. First, the test system and data samples for neural network training are presented. Then, the validity of HTSAC framework is demonstrated and compared with other alternatives. The experiments are performed using the hardware-in-loop platform shown in Fig. 10. The computing platform is configured with CPU i5-6400 with 16G memory capacity with Python and TensorFlow powering the training and calculation of the HTSAC framework.

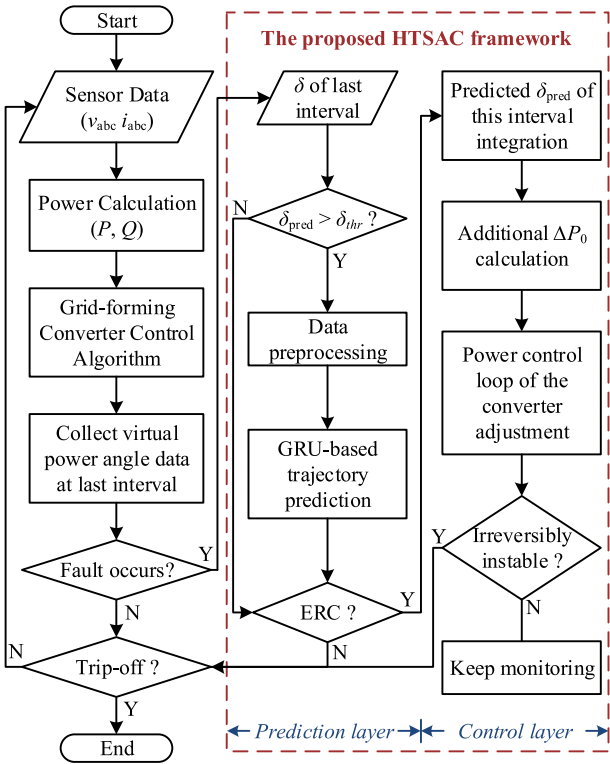
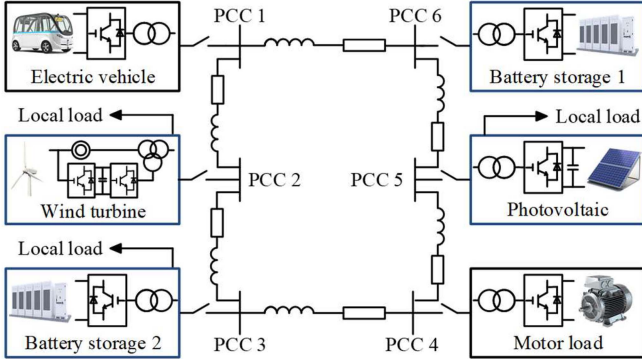
Fig. 7. Flowchart of the proposed HTSAC framework at the  $i$  th interval.

Fig. 8. Topology of the 10kV islanded microgrid in south China [32], [33], [34].

#### A. Validation Object and Sample Generation

To acquire enough data for validation, the training data are generated as follows.

First, the full-order simulation model of the grid-forming converters is established for integrating BESS in the IEEE 14-bus system. The original synchronous generators in the topology are replaced by renewable energy resources like photovoltaics and wind turbines. In particular, the grid-forming converters equipped with BESS are connected to Buses 1 and 2. The grid-feeding converters equipped with photovoltaics are connected to Buses 6 and 8, while Bus 3 integrates the grid-feeding converter with wind power. A three-phase grounded fault is set to occur at different positions of lines and buses, i.e., 25%, 50%, 75% of Lines 1-2, 1-5, 2-5, and Buses 1, 2, 5. The fault is cleared at  $t_c$ , where  $t_c$  is varied between

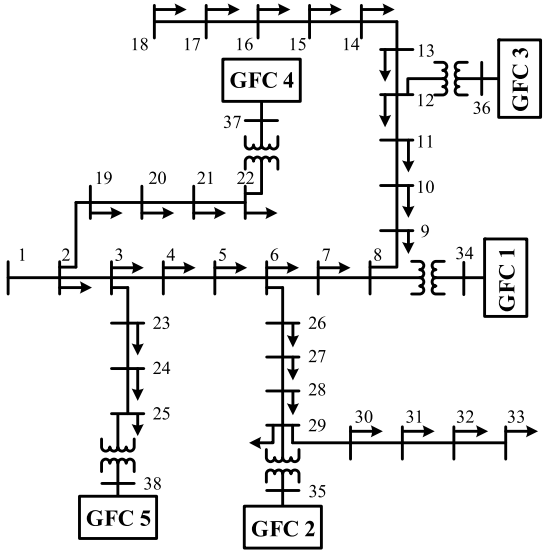


Fig. 9. Topology of the 38-bus islanded microgrid [35].



Fig. 10. Hardware-in-loop platform for validating the proposed HTSAC framework.

0.1- 0.3s. The output active power of the grid-forming converter is varied from 80% of rated value to 120%, with reactive power derived from active power using a constant power factor. Different from the synchronous generators in bulk power systems, the current saturation must be considered for grid-forming converters, where the limitation is set as 2 times the rated value.

Hence, 300 cases in total are generated, and 15000 sets of the virtual power angle trajectory of converters are recorded for training. Here, 60% of data are used for training, 20% for validation, and the remaining 20% are used to verify the performance of the trained GRU in the prediction layer of the HTSAC framework. The training epoch is set as 150, the batch size is set as 64 and the optimizer is adaptive moment estimation.

#### B. Prediction Performance in HTSAC

Here, the grid search method is adopted to verify the performance of the optimal prediction layer of the HTSAC framework. The input horizon and the neuron numbers are selected as independent variables for grid search, the values are

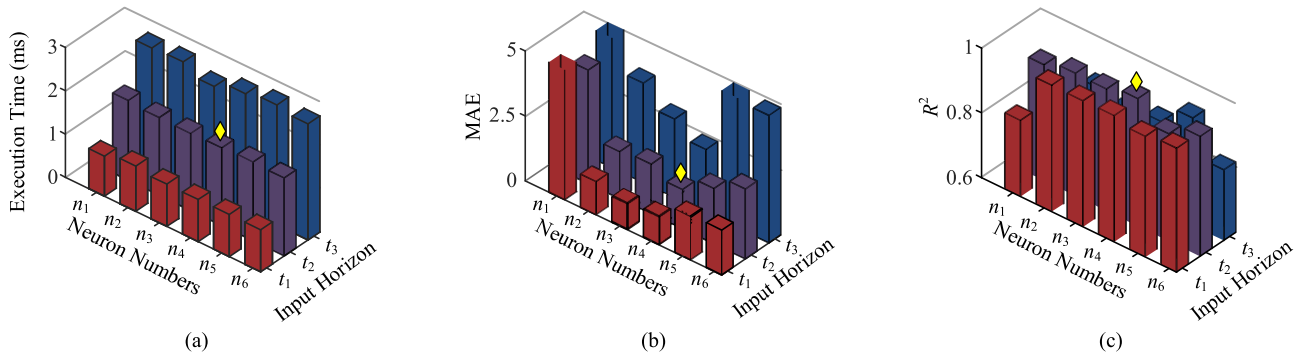


Fig. 11. Validation of the GRU neural network performance in the prediction layer through the grid search method. The cuboid marked with yellow diamond is the neural network used in the proposed HTSAC framework. (a) The execution time for each neural network. (b)  $MAE$  of each neural network. (c)  $R^2$  of each neural network.

TABLE III  
LIST OF NEURAL NETWORKS FOR PREDICTION LAYER

No.	Network	Neuron number $n_i$	Input horizon $t_i$	No.	Network	Neuron number $n_i$	Input horizon $t_i$
1	MLP	200	200 ms	12	GRU	150	200 ms
2	RNN	200	200 ms	13		200	200 ms
3	LSTM	200	200 ms	14		250	200 ms
4		50	100 ms	15		300	200 ms
5		100	100 ms	16		50	300 ms
6		150	100 ms	17		100	300 ms
7	GRU	200	100 ms	18		150	300 ms
8		250	100 ms	19		200	300 ms
9		300	100 ms	20		250	300 ms
10		50	200 ms	21		300	300 ms
11		100	200 ms				

TABLE IV  
COMPARISON OF DIFFERENT NEURAL NETWORKS

Network No.	1	2	3	13
Testing time (per sample)	1.2ms	1.4ms	2.6ms	2.0ms
MAE	10.12	2.957	2.779	1.81
$R^2$	-5.836	0.832	0.923	0.991

listed in Table III, with their performance shown in Fig. 11. The neuron numbers  $n = [n_1, n_2, n_3, n_4, n_5, n_6] = [50, 100, 150, 200, 250, 300]$ , and the input horizon  $t = [t_1, t_2, t_3] = [100, 200, 300]$ . Other neural networks including, MLP (multilayer perception neural network), RNN, and LSTM, are compared with the GRU utilized in this work.

The test set consists of the following samples: half of the samples are from the real islanded microgrids when a three-phase grounded fault occurs at PCC2, 3, and 6, respectively. The remaining samples are from the 38-bus microgrid whose faults are set at five different buses, i.e., buses 8, 11, 20, 25, 27, once a time.

1) *Comparison of Different Neural Networks:* The alternative neural networks share the same neuron numbers and input horizon with the GRU of No. 13. The comparative results listed in Table IV validate the performance of the proposed GRU-based prediction layer.

The MLP-based prediction layer has the fastest speed but the lowest accuracy. RNN is the classical method which has the fewest trainable parameters and the shortest training time.

But its  $MAE$  is rather excessive. The structure of GRU is simpler than that of LSTM; for example, the LSTM-based prediction layer has 181,700 trainable parameters, but the GRU-based prediction layer has only 141,300 with the same input horizon and neuron numbers. Moreover, the required time for the GRU training and prediction is faster than that of the LSTM neural network used in [21]. There are 28% more parameters in LSTM than in GRU, but the execution time is 30% longer than that of the proposed GRU-based prediction layer. Additionally, more parameters do not introduce a better performance. The  $R^2$  metric indicates that the GRU-based prediction layer performs better than the alternative neural network listed here. Thus, the GRU neural network is considered a practical choice.

2) *Impact of Different Neuron Numbers:* The number of neurons influences the execution time and the performance of the proposed HTSAC framework. The proper neuron numbers can avoid the GRU underfitting and overfitting issues.

The GRU prediction layers with different number of neurons in the proposed HTSAC are compared in Fig. 11. The execution time increases gradually by increasing the number of neurons when the input horizon is constant. However, the increase in the number of neurons does not affect the execution time as much as the input horizon. As depicted in Figs. 11(b)-(c), the performance is the best when the number of neurons reaches around 200. Therefore, the number of neurons is set as 200 here.

3) *Impact of Input Horizon Length:* Three input horizon lengths are compared in Fig. 11. Similar to the optimal selection of the number of neurons, the input horizon is compared from the execution time and the performance of the fitting trajectory.

Here, the execution time increases by increasing the input horizon length. However, the adjustment in execution time is manageable as compared with the predicted time length. From this point of view, it seems that setting the time horizon as 300ms is the best. However, the 300ms does not achieve the best prediction performance. The minimal value of  $R^2$  appears at GRU of No. 13, whose input horizon is optimized according to the active power control loop time scale. Meanwhile, the  $MAE$  of GRU No. 13 is the second smallest among all samples. Accordingly, the best choice of input horizon is

TABLE V  
FILE SIZES AND TRAINING TIME OF NEURAL NETWORKS

Network No.	1	2	3	13
Training time (s)	77	986	4395	3337
Weight file size (KB)	338	123	390	301
Structure file size (KB)	1	1	1	1

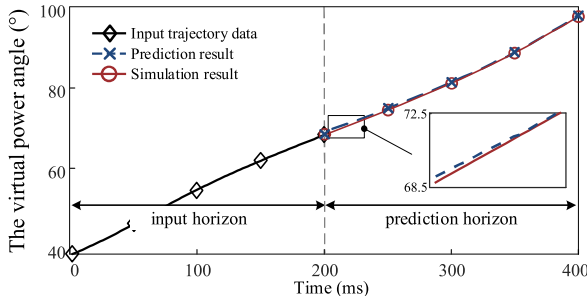


Fig. 12. Virtual power angle trajectories and the output of prediction layer.

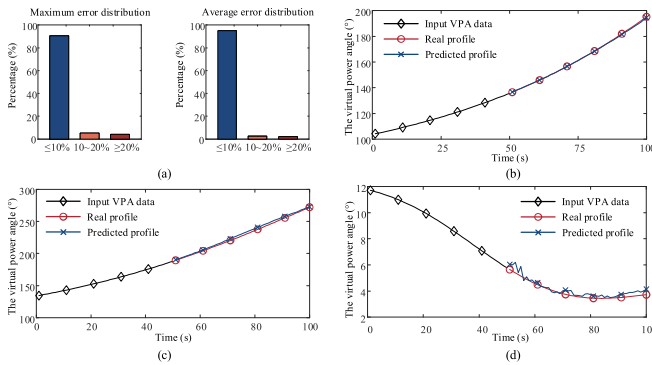


Fig. 13. Virtual power angle trajectories and the error distribution of the 38-bus microgrid. (a) Maximum and average error distributions. (b)-(d) are three stages of trajectories in different cases.

200ms for the GRU-based prediction layer, with its number of neurons set as 200. One of the virtual power angle trajectories predicted by the GRU is illustrated in Fig. 12. Fig. 13 illustrates the prediction results in the 38-bus microgrid, where the maximum error and average error of most test samples is below 10%. Fig. 13(b)-(d) shows three trajectories in different processes, including virtual power angle acceleration increasing, unstable and stable cases. The accurate prediction guarantees in-time emergency control and a stable microgrid operation.

*4) Comparison of the Computational Requirement:* Different from large data-driven models in computer science fields, the proposed HTSAC framework only needs to process matrixed temporal values. The comparison of these algorithms is listed in Table V. Though the proposed HTSAC framework has the second longest training time among these four neural networks, the time-consuming training process is carried out offline. Moreover, the file size of weight matrices and neural network structure of the proposed HTSAC framework only takes up less than 400KB of space, which is lightweight for practical use for a data-driven method.

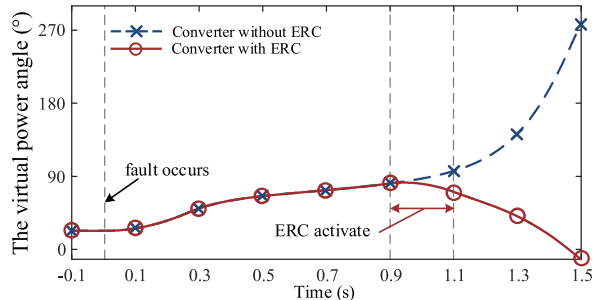


Fig. 14. Virtual power angle trajectories of the grid-forming converter before and after the application of the proposed ERC strategy.

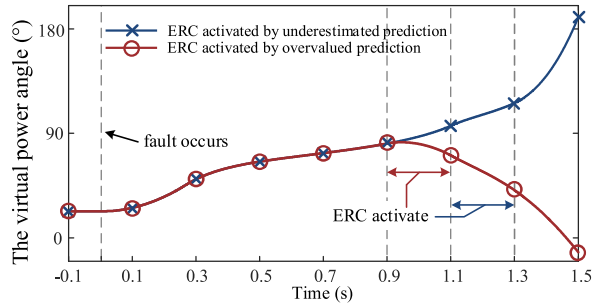


Fig. 15. Comparison of virtual power angle trajectories of grid-forming converters using different prediction layers in the HTSAC framework.

### C. Performance of the ERC Strategy in HTSAC

The Simulink models are established based on the islanded microgrid shown in Figs. 8 and 9 for validating the proposed GRU-based HTSAC framework. First, a three-phase ground fault is placed at PCC6 of the microgrid in Fig. 8 which lasts 0.252s. This is a critical case of the islanded microgrid to show the effectiveness of ERC in the proposed HTSAC, i.e., 0.25s is the critical clearing time of this case. Considering delay and execution times, the trajectory of the grid-forming converter is predicted to be around 0.1s after the ERC signal. The threshold in this work is  $\pi/2$ . The HTSAC framework predicts that the virtual power angle will exceed the threshold in the next interval. The ERC strategy is activated in 0.9s after the fault, which has lasted 0.2s. As illustrated in Fig. 14, the increase in virtual power angle is suppressed significantly by implementing the proposed HTSAC control layer. At the end of the ERC strategy, the virtual power angle profile is changed into the process of recovering from fault. The transient stability of the BESS interface grid-forming converter is thus ensured.

Fig. 15 illustrates the virtual power angle trajectories of the BESS interface grid-forming converter, where the ERC strategies are activated by prediction layers at different moments. Accordingly, the prediction layer trained by the quantile loss ( $\gamma = 0.9$ ) instructs the timely activation of the ERC for the grid-forming converter. The prediction layer trained by the quantile loss ( $\gamma = 0.1$ ) misses predicting the instability, who activates the ERC 0.2s later. As a consequence, the grid-forming converter eventually loses synchronism even though the ERC strategy is applied. This experiment has validated that the proposed HTSAC design is necessary and effective for ensuring the microgrid transient stability.

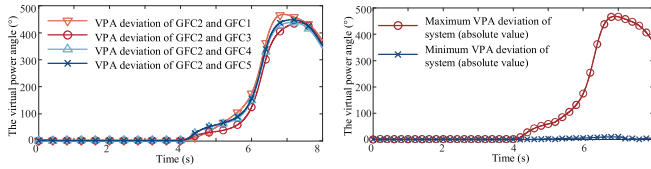


Fig. 16. Virtual power angle deviations of grid-forming converters without the ERC strategy for stabilizing the 38-bus microgrid.

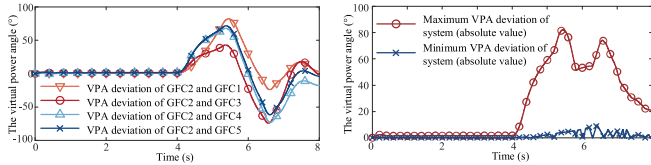


Fig. 17. Virtual power angle deviations of grid-forming converters with the ERC strategy for stabilizing the 38-bus microgrid.

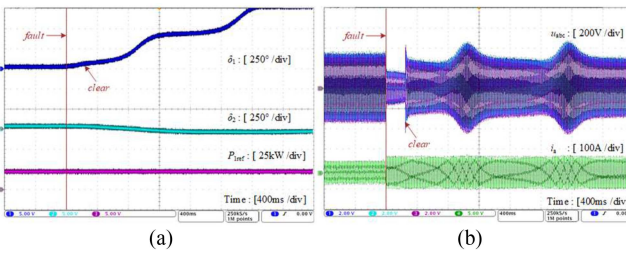


Fig. 18. Experimental comparisons of grid-forming converter results. With no emergency control strategy, the grid-forming converter for integrating BESS 1 loses synchronism.

Then, the proposed HTSAC framework is further validated in the 38-bus microgrid. Figs. 16 and 17 illustrate the relative virtual power angle deviation of each grid-forming converter with and without the HTSAC framework. To maintain the transient stability after a large disturbance in the 38-bus microgrid, the grid-forming converters should retain their coherency, i.e., maximum power angle deviation of each grid-forming converter should be less than a set threshold. When the proposed HTSAC framework is activated, the maximum virtual power angle deviations are those between No. 2 converter and the others, which is still less than  $\pi/2$  denoting that the 38-bus microgrid has maintained its transient stability as shown in Fig. 17.

Figs. 18-20 show the experimental results of the hardware-in-loop of the real islanded microgrid. The grid-forming converter is unstable about 1s after the three-phase ground fault is cleared without the ERC strategy.

The comparisons are illustrated in Figs. 19 and 20 indicating that the trained HTSAC framework trained is able to instruct the timely ERC strategy. The two grid-forming converters utilize ERC strategies after fault, while the converter in Fig. 20 is unstable for taking ERC one period late. Consequently, an undetected transient stability would lead to missing the optimal time to take the ERC strategy. The simulation and the experimental results validate the necessity of training the prediction layer with the proposed method and the effectiveness of the proposed ERC strategy in substantiating the microgrid transient stability.

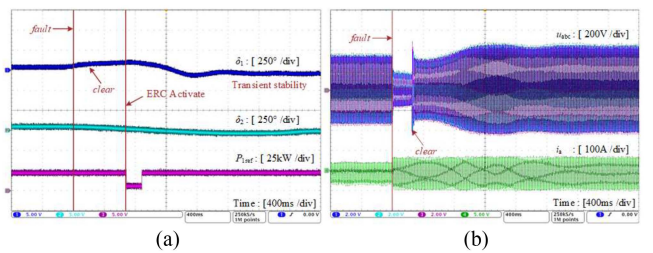


Fig. 19. Experimental results of the HTSAC framework trained by the quantile loss function ( $\gamma = 0.9$ ). (a) Virtual power angle trajectories and the active power reference. (b) Phase A voltage and current of the grid-forming converter.

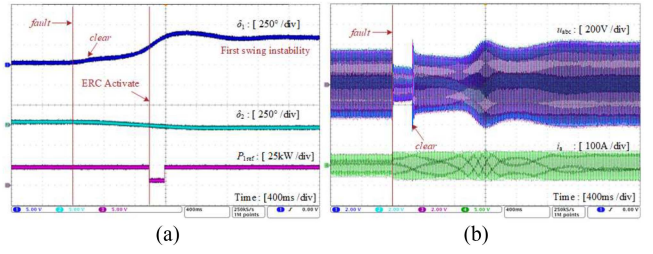


Fig. 20. Experimental results of the HTSAC framework trained by the quantile loss function ( $\gamma = 0.1$ ). (a) The virtual power angle trajectories and the active power reference. The ERC is applied 200ms later than that in Fig. 19. (b) Phase A voltage and current of the grid-forming converter.

#### D. Discussion

Considering the case study results for the real islanded microgrid and the 38-bus microgrid, the proposed HTSAC framework has shown its effectiveness and superiority in enhancing the transient stability.

Since stable operation is a basic requirement of an islanded microgrid, acquiring the state and instructing the corresponding control strategies is an essential concern for the microgrid operation. The proposed HTSAC framework responds to the concern in three respects: (1) A unified solution from the assessment to the action is achieved by the proposed organic framework, i.e., the continuous TSA predicts the virtual power angle trajectory for quantitatively determining the ERC signal, as illustrated in Figs. 14-15 and 18-20. (2) One of the key parameters in the proposed HTSAC framework is quantitatively optimized according to the time scale, which eliminates the commonly used time-consuming trial-and-error method. The approach makes the proposed HTSAC framework more portable as demonstrated in Fig. 11 which confirms the superiority of the optimized input horizon. (3) Owing to the predicted high-precision trajectory, ERC is able to adaptively engage an effective control signal to stabilize the system which is appropriate for the current operating state, as demonstrated in both the 10kV islanded microgrid with critical stability (Figs. 14 and 15) and the 38-bus microgrid (Figs. 16 and 17).

## V. CONCLUSION

In this work, an HTSAC framework consisting of a prediction layer and a control layer is proposed. The proposed HTSAC framework can predict the virtual power angle trajectory precisely. By leveraging the predicted trajectory, a real-time adaptive ERC strategy is activated to avoid the instability of the grid-forming converters which is interfaced

with BESS in islanded microgrids. The proposed HTSAC framework presents the following features:

(1) The proposed HTSAC framework is suitable for online applications because it can predict the transient stability precisely with only one input. The desirable performance of the HTSAC framework is achieved as it only takes 2ms to predict the 200ms data.

(2) The input horizon of the neural network in the prediction layer is optimized by the time scale of the grid-forming converter's power control loop to avoid a low-efficient trial-and-error solution. Accordingly, the proposed HTSAC framework is capable of being generalized to other microgrid operations with a reasonable performance.

(3) The proposed ERC strategy in the control layer of the HTSAC framework combines the transient stability mechanism with the neural network that provides an effective and easy calculation procedure. The proposed ERC strategy adaptively adjusts the power control loop of the BESS interfaced grid-forming converters to facilitate the transient stability of the converters in islanded microgrids.

The microgrid input could include false and noisy data. Therefore, the future work will consider the risks of cyber-attack and focus on enhancing the robustness of the proposed HTSAC framework for microgrid operations.

## REFERENCES

- [1] W. Bao, Q. Wu, L. Ding, S. Huang, and V. Terzija, "A hierarchical inertial control scheme for multiple wind farms with BESSs based on ADMM," *IEEE Trans. Sustain. Energy*, vol. 12, no. 2, pp. 751–760, Apr. 2021.
- [2] Q. Zhou, M. Shahidehpour, A. Paaso, S. Bahramirad, A. Alabdulwahab, and A. Abusorrah, "Distributed control and communication strategies in networked microgrids," *IEEE Commun. Surveys Tuts.*, vol. 22, no. 4, pp. 2586–2633, 4th Quart., 2020.
- [3] L. Huang et al., "Grid-synchronization stability analysis and loop shaping for PLL-based power converters with different reactive power control," *IEEE Trans. Smart Grid*, vol. 11, no. 1, pp. 501–516, Jan. 2020.
- [4] E. Rokrok, T. Qoria, A. Bruyere, B. Francois, and X. Guillaud, "Transient stability assessment and enhancement of grid-forming converters embedding current reference saturation as current limiting strategy," *IEEE Trans. Power Syst.*, vol. 37, no. 2, pp. 1519–1531, Mar. 2022.
- [5] Q. Zhou, Z. Tian, M. Shahidehpour, X. Liu, A. Abdulwhab, and A. Abusorrah, "Optimal consensus-based distributed control strategy for coordinated operation of networked microgrids," *IEEE Trans. Power Syst.*, vol. 35, no. 3, pp. 2452–2462, May 2020.
- [6] D. J. Ryan, R. Razzaghi, H. D. Torresan, A. Karimi, and B. Bahrani, "Grid-supporting battery energy storage systems in islanded microgrids: A data-driven control approach," *IEEE Trans. Sustain. Energy*, vol. 12, no. 2, pp. 834–846, Apr. 2021.
- [7] Q. Zhou, M. Shahidehpour, A. Alabdulwahab, A. Abusorrah, L. Che, and X. Liu, "Cross-layer distributed control strategy for cyber resilient microgrids," *IEEE Trans. Smart Grid*, vol. 12, no. 5, pp. 3705–3717, Sep. 2021.
- [8] D. Osiopov and K. Sun, "Adaptive nonlinear model reduction for fast power system simulation," *IEEE Trans. Power Syst.*, vol. 33, no. 6, pp. 6746–6754, Nov. 2018.
- [9] S. Jin, Z. Huang, R. Diao, D. Wu, and Y. Chen, "Comparative implementation of high performance computing for power system dynamic simulations," *IEEE Trans. Smart Grid*, vol. 8, no. 3, pp. 1387–1395, May 2017.
- [10] Z. K. Shuai, C. Shen, X. Liu, Z. Y. Li, and Z. J. Shen, "Transient angle stability of virtual synchronous generators using Lyapunov's direct method," *IEEE Trans. Smart Grid*, vol. 10, no. 4, pp. 4648–4661, Jul. 2019.
- [11] F. Andrade, K. Kampouropoulos, L. Romeral, J. C. Vasquez, and J. M. Guerrero, "Study of large-signal stability of an inverter-based generator using a Lyapunov function," in *Proc. IECON*, Dallas, TX, USA, 2014, pp. 1840–1846.
- [12] T. Huang, S. Gao, and L. Xie, "A neural Lyapunov approach to transient stability assessment of power electronics-interfaced networked microgrids," *IEEE Trans. Smart Grid*, vol. 13, no. 1, pp. 106–118, Jan. 2022.
- [13] M. Kabalan, P. Singh, and D. Niebur, "Nonlinear Lyapunov stability analysis of seven models of a DC/AC droop controlled inverter connected to an infinite bus," *IEEE Trans. Smart Grid*, vol. 10, no. 1, pp. 772–781, Jan. 2019.
- [14] D. J. Sobajic and Y.-H. Pao, "Artificial neural-net based dynamic security assessment for electric power systems," *IEEE Trans. Power Syst.*, vol. 4, no. 1, pp. 220–228, Feb. 1989.
- [15] T. Guo and J. V. Milanović, "Probabilistic framework for assessing the accuracy of data mining tool for online prediction of transient stability," *IEEE Trans. Power Syst.*, vol. 29, no. 1, pp. 377–385, Jan. 2014.
- [16] W. Hu et al., "Real-time transient stability assessment in power system based on improved SVM," *J. Mod. Power Syst. Clean Energy*, vol. 7, no. 1, pp. 26–37, Jan. 2019.
- [17] Q. Li, Y. Xu, and C. Ren, "A hierarchical data-driven method for event-based load shedding against fault-induced delayed voltage recovery in power systems," *IEEE Trans. Ind. Informat.*, vol. 17, no. 1, pp. 699–709, Jan. 2021.
- [18] A. Gupta, G. Gurrala, and P. S. Sastry, "An online power system stability monitoring system using convolutional neural networks," *IEEE Trans. Power Syst.*, vol. 34, no. 2, pp. 864–872, Mar. 2019.
- [19] X. Li, Z. Yang, P. Guo, and J. Cheng, "An intelligent transient stability assessment framework with continual learning ability," *IEEE Trans. Ind. Informat.*, vol. 17, no. 12, pp. 8131–8141, Dec. 2021.
- [20] B. Li, J. Wu, L. Hao, M. Shao, R. Zhang, and W. Zhao, "Anti-jitter and refined power system transient stability assessment based on long-short term memory network," *IEEE Access*, vol. 8, pp. 35231–35244, 2020.
- [21] J. J. Q. Yu, D. J. Hill, A. Y. S. Lam, J. Gu, and V. O. K. Li, "Intelligent time-adaptive transient stability assessment system," *IEEE Trans. Power Syst.*, vol. 33, no. 1, pp. 1049–1058, Jan. 2018.
- [22] J. Gonzalez, P. N. Papadopoulos, J. V. Milanović, G. Peskir, and J. Moriarty, "Risk-constrained minimization of combined event detection and decision time for online transient stability assessment," *IEEE Trans. Smart Grid*, vol. 12, no. 5, pp. 4564–4572, Sep. 2021.
- [23] Z. Shi et al., "Convolutional neural network-based power system transient stability assessment and instability mode prediction," *Appl. Energy*, vol. 263, Apr. 2020, Art. no. 114586.
- [24] J. D. Pinzón and D. G. Colomé, "Real-time multi-state classification of short-term voltage stability based on multivariate time series machine learning," *Int. J. Electr. Power Energy Syst.*, vol. 108, pp. 402–414, Jun. 2019.
- [25] A. K. Singh and M. Fozdar, "Event-driven frequency and voltage stability predictive assessment and unified load shedding," *IET Gener. Transm. Distrib.*, vol. 13, no. 19, pp. 4410–4420, 2019.
- [26] S. A. Siddiqui, K. Verma, K. R. Niazi, and M. Fozdar, "A unified control scheme for power system transient stability enhancement through preventive and emergency control," *Int. J. Electr. Power Energy Syst.*, vol. 26, no. 2, pp. 365–383, 2016.
- [27] Q. Wang, F. Li, Y. Tang, and Y. Xu, "Integrating model-driven and data-driven methods for power system frequency stability assessment and control," *IEEE Trans. Power Syst.*, vol. 34, no. 6, pp. 4557–4568, Nov. 2019.
- [28] J. Chang, Y. Du, E. G. Lim, H. Wen, X. Li, and L. Jiang, "Coordinated frequency regulation using solar forecasting based virtual inertia control for islanded microgrids," *IEEE Trans. Sustain. Energy*, vol. 12, no. 4, pp. 2393–2403, Oct. 2021.
- [29] S. Zhang, T. Liang, T. Cheng, and V. Dinavahi, "Machine learning based modeling for real-time inferencer-in-the-loop hardware emulation of high-speed rail microgrid," *IEEE Trans. Emerg. Sel. Topics Ind. Electron.*, vol. 3, no. 4, pp. 920–932, Oct. 2022.
- [30] J. Han, "From PID to active disturbance rejection control," *IEEE Trans. Ind. Electron.*, vol. 56, no. 3, pp. 900–906, Mar. 2009.
- [31] S. Boyd and L. Vandenberghe, *Convex Optimization*. Cambridge, U.K.: Cambridge Univ. Press, 2004.
- [32] L. He, Y. Li, X. Chu, Z. Shuai, Y. Peng, and Z. J. Shen, "Single-phase to ground fault line identification for medium voltage islanded microgrids with neutral ineffectively grounded modes," *IEEE Trans. Smart Grid*, vol. 13, no. 6, pp. 4312–4326, Nov. 2022.

- [33] L. He, Z. Shuai, X. Chu, W. Huang, Y. Feng, and Z. J. Shen, "Waveform difference feature-based protection scheme for islanded microgrids," *IEEE Trans. Smart Grid*, vol. 12, no. 3, pp. 1939–1952, May 2021.
- [34] X. Shen, J. Ge, W. Huang, L. He, and Z. Shuai, "Secondary power sharing control strategy for hybrid AC/DC microgrid via maximum power coordination factor," in *Proc. EI2*, Changsha, China, 2019, pp. 1938–1943.
- [35] F. Mumtaz, M. H. Syed, M. A. Hosani, and H. H. Zeineldin, "A novel approach to solve power flow for islanded microgrids using modified Newton Raphson with droop control of DG," *IEEE Trans. Sustain. Energy*, vol. 7, no. 2, pp. 493–503, Apr. 2016.



**Yang Shen** (Graduate Student Member, IEEE) received the B.S. degree in electrical engineering from Jiangsu University, Zhenjiang, China, in 2018. He is currently pursuing the Ph.D. degree with the College of Electrical and Information Engineering, Hunan University, Changsha, China. His research interests include application of artificial intelligence in power system, stability analysis and assessment, and data-driven control of microgrid system.



**Quan Zhou** (Senior Member, IEEE) received the B.S. and M.S. degrees from the Department of Electrical Engineering, Shanghai Jiao Tong University, Shanghai, China, in 2011 and 2016, respectively, and the Ph.D. degree from Illinois Institute of Technology, Chicago, IL, USA, in 2019. He is currently a Professor with the College of Electrical and Information Engineering, Hunan University, Changsha, China. He has published more than 50 top-tier journal papers, including three ESI highly cited papers. His research interests include satellite Internet and its applications, microgrids, coordinated control and communication, and cybersecurity. He is an Associate Editor of IEEE TRANSACTIONS ON SMART GRID and IEEE POWER AND ENGINEERING LETTERS.



**Lipeng Zhu** (Member, IEEE) received the B.S. degree in electrical engineering from the Huazhong University of Science and Technology, Wuhan, China, in 2012, the M.S. degree in electrical engineering from Wuhan University, Wuhan, in 2015, and the Ph.D. degree in electrical engineering from Tsinghua University, Beijing, China, in 2018. He was a Postdoctoral Fellow/Senior Research Assistant with The University of Hong Kong, Hong Kong, from 2018 to 2021. He is currently a Professor with Hunan University, Changsha, China. His research interests mainly include spatial-temporal energy data analysis, IoT data management and analytics in smart grids, synchrophasor measurement technologies, and data-driven power system stability and control.



**Yelun Peng** (Member, IEEE) received the B.S. degree in electrical and information engineering from Changsha University of Science and Technology, Changsha, and the Ph.D. degree in electrical engineering from the College of Electrical and Information Engineering, Hunan University, Changsha. In 2017, he was a guest Ph.D. student with the Department of Energy Technology, Aalborg University, Denmark. From September 2019 to August 2021, he was a Research Fellow with the School of Electrical and Electronic Engineering, University. Since 2020, he has been a Postdoctoral Researcher with Hunan University. His research interests include modeling and stability analysis of microgrids.



**Z. John Shen** (Fellow, IEEE) received the B.S. degree in electrical engineering from Tsinghua University, China, in 1987, and the M.S. and Ph.D. degrees in electrical engineering from Rensselaer Polytechnic Institute, Troy, NY, USA, in 1991 and 1994, respectively. He was on faculty of the University of Michigan at Dearborn from 1999 to 2004, and the University of Central Florida from 2004 to 2012. In 2013, he joined the Illinois Institute of Technology as the Grainger Chair Professor in Electrical and Power Engineering. He is currently a Professor and the Director of the School of Mechatronic Systems Engineering, Simon Fraser University, Surrey, BC, Canada. He has been an Active Volunteer in the IEEE Power Electronics Society, and has served as the VP of Products 2009–2012, an Associate Editor and a Guest Editor-in-Chief for the IEEE TRANSACTIONS ON POWER ELECTRONICS, and the technical program chair and the general chair of several major IEEE conferences.



**Zhilang Shuai** (Senior Member, IEEE) received the B.S. and Ph.D. degrees in electrical engineering from the College of Electrical and Information Engineering, Hunan University, Changsha, China, in 2005 and 2011, respectively. From 2009 to 2012, he was an Assistant Professor with Hunan University, where he was an Associate Professor in 2013, and a Professor in 2014. His research interests include power quality control, power electronics, and microgrid stability analysis and control. He received the 2010 National Scientific and Technological Awards of China, the 2012 Hunan Technological Invention Awards of China, and the 2007 Scientific and Technological Awards from the National Mechanical Industry Association of China. He is an Associate Editor of the *CSEE Journal of Power and Energy Systems* and *Chinese Journal of Electrical Engineering*.



**Mohammad Shahidehpour** (Life Fellow, IEEE) received the Honorary Doctorate degree in electrical engineering from the Polytechnic University of Bucharest, Romania. He is the Bodine Chair Professor and the Director of the Robert W. Galvin Center for Electricity Innovation, Illinois Institute of Technology, Chicago, IL, USA. He is listed as a Highly Cited Researcher on the Web of Science. He is a Fellow of the American Association for the Advancement of Science and the National Academy of Inventors, Laureate of KIA (Khwarizmi International Award), and an Elected Member of the U.S. National Academy of Engineering.